Fabrication of Carbon-Encapsulated Mono- and Bimetallic (Sn and Sn/Sb Alloy) Nanorods. Potential Lithium-Ion Battery Anode Materials

Sang Ho Lee,[†] Martin Mathews,[†] Hossein Toghiani,[‡] David O. Wipf,[†] and Charles U. Pittman, Jr.*,[†]

Department of Chemistry and Dave C. Swalm School of Chemical Engineering, Mississippi State University, Mississippi 39762

Received March 6, 2009. Revised Manuscript Received April 10, 2009

Novel carbon-encapsulated mono- and bimetallic (Sn and Sn/Sb alloy) core−shell nanorods were synthesized as potential anode materials for future lithium-ion batteries by a reductive, thermochemical vapor deposition at different acetylene/nitrogen (1:9) gas flow rates (20, 30, and 200 sccm) between 750 and 810 °C over SnO_2/Sb_2O_{10} and SnO_2 nanopowders. Their morphologies and structures were characterized by SEM and TEM. Nanorod morphologies varied depending on the acetylene flow rate. The outer carbon layer thickened with time. More irregular nonuniform growth occurred at longer growth periods at 810 °C, giving spherical, conical, bulblike, and/or lumpy structures containing various amounts of metal. Sharp powder X-ray diffraction (XRD) peaks proved that well-crystallized Sn metal and Sn/Sb alloy formed within the carbon shells. Certain conditions generated some SnO_2 within the carbon shell. X-ray photoelectron spectroscopy (XPS) determined the elements present and their oxidation states. The main carbon peak in all nanorods was graphitic carbon. C_{1s} and O_{1s} high-resolution spectra confirmed a variety of oxygenated carbon species were present on the outer carbon surface region. The metallic core in the carbon-encased Sn nanorods contained Sn metal, SnO_2, and possibly SnO (XPS), in good agreement with XRD measurements.

Introduction

The anode materials in Li-ion batteries typically have used natural graphite, which consists of layers (or sheets) of hexagonal arrays of sp^2-hybridized carbon (benzene rings). Graphite's high theoretical specific capacity for Li^+ intercalation of 372 mAh/g[1] and its high electrical conductivity led to its use as the anode in rechargeable Li ion batteries. The specific energy capacity of graphite is partially limited by the thermodynamically determined equilibrium saturation composition of LiC_6.[1]

For a decade, carbon nanotubes (CNTs) have been suggested as an alternative to graphite anode materials.[2−20] Their unique structure, large surface area, and high electrical conductivity are promising features for high-energy-density rechargeable Li-ion battery anodes. CNTs can potentially have a higher saturation composition than graphite by accommodating guest species both within and between the nanotubes.[3]

Tin (Sn) is also a promising anode material for Li-ion batteries because of its high theoretical Li storage capacity.[18,19,21−26] Tin alloys with lithium, giving an extremely high storage

* Corresponding author. Phone: (662) 325-7616. E-mail: CPittman@ra.msstate.edu.
[†] Department of Chemistry, Mississippi State University.
[‡] Dave C. Swalm School of Chemical Engineering, Mississippi State University.

(1) Zheng, T.; Zhong, Q.; Dahn, J. R. *J. Electrochem. Soc.* **1995**, *142*, L211.
(2) Che, G.; Lakshmi, B. B.; Fisher, E. R.; Martin, C. R. *Nature* **1998**, *393*, 346.
(3) Gao, B.; Kleinhammes, A.; Tang, X. P.; Bower, C.; Fleming, L.; Wu, Y.; Zhou, O. *Chem. Phys. Lett.* **1999**, *307* (3−4), 153.
(4) Gao, B.; Bower, C.; Lorentzen, J. D.; Fleming, L.; Kleinhammes, A.; Tang, X. P.; McNeil, L. E.; Wu, Y.; Zhou, O. *Chem. Phys. Lett.* **2000**, *327*, 69.
(5) Shimoda, H.; Gao, B.; Tang, X. P.; Kleinhammes, A.; Fleming, L.; Wu, Y.; Zhou, O. *Phys. Rev. Lett.* **2002**, *88*, 1–015502.
(6) Yang, S.; Song, H.; Chen, X.; Okotrub, A. V.; Bulusheva, L. G. *Electrochim. Acta* **2007**, *52*, 5286.
(7) Wang, Q.; Liu, L.; Chen, L.; Huang, X. *J. Electrochem. Soc.* **2004**, *151*, A1333.
(8) Eom, J. Y.; Kwon, H. S.; Liu, J.; Zhou, O. *Carbon* **2004**, *42*, 2589.
(9) Meunier, V.; Kephart, J.; Roland, C.; Bernholc, J. *Phys. Rev. Lett.* **2002**, *88*, 075506.
(10) Eom, J. Y.; Kwon, H. S.; Liu, J.; Zhou, O. *Carbon* **2004**, *42*, 2589.
(11) Wu, G. T.; Chen, M. H.; Zhu, G. M.; You, J. K.; Lin, Z. G.; Zhang, X. B. *J. Solid State Electrochem.* **2003**, *7*, 129.
(12) Sharon, M.; Hsu, W. K.; Kroto, H. W.; Walton, D. R. M.; Kawahara, A.; Ishihara, T.; Takita, Y. *J. Power Sources* **2002**, *104*, 148.
(13) Wang, G. X.; Ahn, J.; Yao, J.; Lindsay, M.; Liu, H. K.; Dou, S. X. *J. Power Sources* **2003**, *119*, 16.
(14) Lemos, V.; Guerini, S.; Lala, S. M.; Montoro, L. A.; Rosolen, J. M. *Microelectron. J.* **2005**, *36*, 1020.
(15) Chen, W. X.; Lee, J. Y.; Liu, Z. L. *Electrochem. Commun.* **2002**, *4*, 260.
(16) Guo, Z. P.; Zhao, Z. W.; Liu, H. K.; Dou, S. X. *Carbon* **2005**, *43*, 1392.
(17) Xie, J.; Varadan, V. K. *Mater. Chem. Phys.* **2005**, *91*, 274.
(18) Kumar, T. P.; Ramesh, R.; Lin, Y. Y.; Fey, G. T. *Electrochem. Commun.* **2004**, *6*, 520.
(19) Wang, Y.; Zeng, H. C.; Lee, J. Y. *Adv. Mater.* **2006**, *18*, 645.
(20) Wang, Y.; Yang, I. *Angew. Chem., Int. Ed.* **2006**, *45*, 7039.
(21) Wang, Y.; Lee, J. Y. *J. Phys. Chem. B* **2004**, *108*, 17832.
(22) Wang, Y.; Lee, J. Y.; Zeng, H. C. *Chem. Mater.* **2005**, *17*, 3899.
(23) Veeraraghavan, B.; Durairajan, A.; Haran, B.; Popov, B.; Guidotti, R. *J. Electrochem. Soc.* **2002**, *149*, 6–A675.
(24) Ying, Z.; Wan, Q.; Cao, H.; Song, Z. T.; Feng, S. L. *Appl. Phys. Lett.* **2005**, *87*, 113108.
(25) Park, M. S.; Wang, G. X.; Kang, Y. M.; Wexler, D.; Dou, S. X.; Liu, H. K. *Angew. Chem., Int. Ed.* **2007**, *46*, 750.
(26) Li, N.; Martin, C. R. *J. Electrochem. Soc.* **2001**, *148*, A164.

10.1021/cm900640u CCC: $40.75
Published on Web 05/04/2009

capacity (theoretical value: ~790 mAh/g vs 372 mAh/g of graphite).[21,22] However, tin powder loses capacity rapidly when used alone in the anode due to severe volume expansion (up to 259%[23]) and contraction during the alloying/dealloying (e.g., charge and discharge) cycles with Li^+ ions. Expansion and contraction leads to pulverization of the anode material during repetitive deep charge and discharge operations, reducing the discharge capacity.

The fragmentation of expanding and contracting particles will depend on particle size. Tin structures in the nanometer size range may not fragment during charge/discharge cycling. Recently, other tin structures have been suggested including SnO_2 nanorods,[21] polycrystalline SnO_2 nanotubes,[22] SnO_2 nanowires,[24,25] CNT-supported SnO_2 nanoparticles,[15−18] and CNT−SnO_2 duplex nanotubes.[19] These oxide structures would be reduced to Sn and then form Sn_xLi_y alloys during the charging cycle. The tubular tin and tin in CNT templates appeared promising in overcoming the pulverization problem caused by volume change during electrochemical reactions. Such structures have shown significant improvement in initial application performance studies.[15−26]

Wang et al.[19] used inner SnO_2/outer CNT duplex nanotubes for reversible lithium anode storage. These SnO_2 nanotubes with uniform CNT skins were prepared by a two-step template deposition method, where tubular porous SnO_2 was prepared by infiltrating nanotin oxide into high-purity alumina (Al_2O_3) membranes containing 200 nm diameter pores. The SnO_2-nanoparticle-filled alumina membrane was then infused by a hydrocarbon gas at high temperatures, generating a carbon layer adjacent to the alumina pore surface encapsulating the SnO_2 nanotubes. These uniform rods were freed by dissolving away the Al_2O_3. They exhibited a high reversible capacity (~540−600 mAh/g) and excellent cyclability (0.0375% capacity loss per cycle). This ability to cycle showed that these nanostructures did not suffer the same fragmentation problems that are observed with the larger-sized particles found in tin powder. However, the infiltration process was particularly difficult and impractical in our hands during repeated attempts to duplicate and scale-up this work.

More recently, Wang et al.[20] generated intermetallic Sn/Sb alloy nanorods encased in carbon from a mixture of commercial antimony oxide and tin oxide (Sb_2O_5/SnO_2) nanoparticles during high-temperature decomposition of acetylene. This process exhibits potential simplicity (one-step process). If the total mass of the metal oxides could be converted into nanorods, scale up might be possible. High specific capacities and good cycling performance were claimed.

We report here the synthesis of two types of carbon-covered mono- and bimetallic (Sn and Sn/Sb alloy) nanorods by a thermochemical vapor deposition method. Commercial mixtures of antimony and tin oxides (Sb_2O_5/SnO_2) nanoparticles or tin(IV) oxide (SnO_2) nanoparticles (~19 nm) were used as the precursors for the growth of bimetallic Sn/Sb alloy or monometallic Sn nanorods, respectively, in a flow of hot (750−810 °C) acetylene diluted in nitrogen. These nanorods were encased in an outer carbon layer. In addition, different product morphologies were observed at different hydrocarbon gas flow rates. The inner metal rod diameters and the outer concentric carbon encapsulating layer thickness could be varied. Acetylene and methane were tried. The morphologies and intermetallic nanorod structures and compositions within the carbon templates were investigated using SEM, TEM, X-EDS, XRD, and XPS studies.

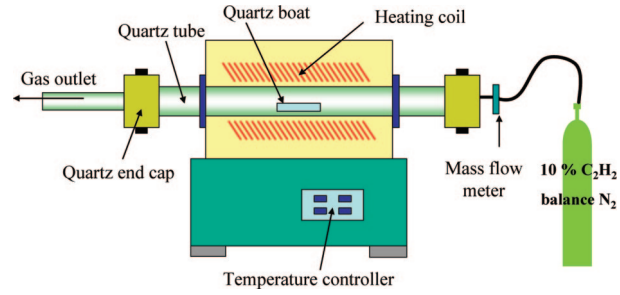

Figure 1. Diagram of the thermal CVD apparatus.

Experimental Section

Materials. Commercial antimony tin oxide nanopowder (ATO, Sb_2O_5·SnO_2, particle size ≈ 19 nm, Sb_2O_5 7−11 wt %, SnO_2 89−93 wt %, Sn/Sb atomic ratio = 8.7 to 14.3) and tin oxide nanopowder, SnO_2, (particle size ~18.3 nm) were obtained from Sigma Aldrich and used without further purification. A quartz reactor tube (1″ OD × 0.75″ ID × 32″ long), a quartz boat, and quartz end-caps were used as the tubular reactor crucible for the thermal chemical vapor deposition (CVD) process. Also, a mass flow controller and a proportional valve controlled the gas flow rates of acetylene in nitrogen (10% C_2H_2 90% N_2, Airgas. Inc.), over the nanopowders in the reactor at 1 atm to grow the nanotubes. This reactor is shown schematically in Figure 1.

Sample Preparation. Both types of inner metallic (Sn and Sn/Sb) carbon-encased nanorods were prepared by thermal chemical vapor deposition (CVD) under the same experimental CVD conditions. The commercial antimony oxide/tin oxide nanoparticles (Sb_2O_5·SnO_2) or tin(IV) oxide nanopowder (SnO_2) were uniformly distributed on a quartz boat in a crucible. The crucible was heated to temperatures from 750 to 810 °C (ramp rate 10 °C/min to 660 and 5 °C/min to 750 or 810 °C) followed by reaction times of 1−8 h under flowing C_2H_2 (20, 30, and 200 sccm, 10% C_2H_2/90% N_2). The crucible was then cooled to room temperature under this same gas mixture. In one example reaction, the weight of the recovered nanorod product powders had doubled (from 0.23 g of SnO_2/Sb_2O_5 charged to 0.48 g of carbon-covered Sn/Sb nanorods). To the eye, black-colored powders were obtained. The bimetallic Sn/Sb/carbon nanorods were prepared at three different gas flow rates (20, 30, and 200 sccm).

Characterization. Surface morphologies of the intermetallic (Sn and Sn/Sb) nanorods encased in carbon were examined by scanning electron microscopy (SEM). Samples were coated with Pt−Au using a Polaron E5100 sputter coater in some cases. A JSM-6500F (JEOL) field emission scanning electron microscope was used at 5.0 kV to 30 kV, employing magnifications of 10 000−100 000×. The nanorod phases were analyzed by X-EDS (Inca-Sight EDS7558 instrument, OXFORD) to determine the approximate local Sn, Sb, O, and C contents of the structures observed in the SEM images.

Transmission electron microscopy (TEM, JEOL JEM-100CX II) was used to identify and characterize the nanorod morphologies and structures. TEM samples were prepared by ultrasonic dispersion in ethanol for several min. A few drops of the suspension were then placed on a copper grid.

Powder X-ray diffraction was performed with nickel-filtered Cu K_α radiation, collecting data between scattering angles (2θ) of 4

and 50° in steps of 0.02°. X-ray photoelectron spectroscopy (XPS) experiments were carried out using aluminum K_α X-ray radiation. All spectra were recorded from 0 to 1100 eV on an instrument equipped with a PHI model 10−360 spherical capacitor energy analyzer and an Omni Focus III small-area lens (800 μm diameter analysis area) and a high-performance channel detector, at a pass energy of 46.95 or 23.50 eV for high-resolution scans. The system pressure was held below 1×10^{-9} Torr.

Results and Discussion

The two types of carbon-covered intermetallic nanorods (Sn and Sn/Sb) in carbon were successfully synthesized by a thermal CVD method. The nanopowder precursors (antimony(V) oxide and tin(IV) oxide) were first reduced to form low-melting metals (Sn/Sb or Sn) by acetylene at temperatures from 750 to 810 °C. These molten metal phases catalyze the growth of nanoscale carbon tubes by C_2H_2 decomposition. The low-melting Sn or Sn/Sb are present as liquid droplets upon reduction in this high temperature region. Carbon tubes then grow upward on this molten surface as H_2 is stripped from acetylene and the carbon graphitizes. Simultaneously, the liquid metal is drawn up into the interior of the CNTs by capillary forces. These carbon tubes are open at the end that is growing from the liquid Sn or Sn/Sb surfaces, generating capillary forces to drive the filling process. At some point this elongation stops and these open ends become covered with carbon. Most of the carbon tubes contained a metal rod inside the external carbon tube, although a small fraction of these carbon tubes were hollow.

Scanning Electron Microscopy (SEM) and X-EDS Analyses. Figure 2 displays SEM images of these rodlike structures. They are recovered from the reactor as black powders. Those shown in Figure 2 were prepared at 750 °C over 4 h under flowing C_2H_2 (20 and 200 sccm, 10% C_2H_2/90% N_2). These surface images show curved rod-shaped products. They were observed to have very rough carbon surfaces. Each product was examined by a fixed magnification (10 000, 30 000, 100 000×) to compare the rod-shaped structures prepared at different C_2H_2 flow rates over the SnO_2/Sb_2O_5 nanopowders. Interestingly, the thickness of the carbon-encapsulated metal rods was substantially greater at the higher (200 sccm) acetylene flow rate (Figure 2A−C vs. E−G). The higher acetylene flow rate led to thicker outer concentric carbon layers and somewhat thinner inner metal rods at 750 °C.

Spot analysis by X-EDS of the nanorods confirmed the presence of C, Sn, and Sb. Spectra D and H in Figure 2 also show X-EDS spectra of the carbon−Sn/Sb nanorods formed at both 200 and 20 sccm acetylene flow rates, using a $SnO_2 \cdot Sb_2O_5$ mole ratio of 0.9:0.1, $(SnO_2)_{0.9}(Sb_2O_5)_{0.1}$. The oxygen peak could be due to small amounts of unreduced metal oxide or surface oxygenated groups on the outer carbon layer. Figure 2L is an X-EDS spectrum of the monometallic Sn nanorods, formed when only SnO_2 was placed in the reactor boat. It exhibits peaks for tin and carbon with a small amount of oxygen. X-EDS-derived elemental analyses of several products were summarized in Table 1 along with average total tube and the inner rod diameters.

The synthesis of bimetallic carbon-encased nanorods (C−Sn/Sb) was also attempted using methane (10% CH_4 and 90% N_2, 20 to 100 sccm) in place of acetylene as a carbon source. Reactions were conducted under the same experimental CVD conditions. An SEM image and an X-EDS spectrum of the product from $Sb_2O_5 \cdot SnO_2$ exposure to CH_4

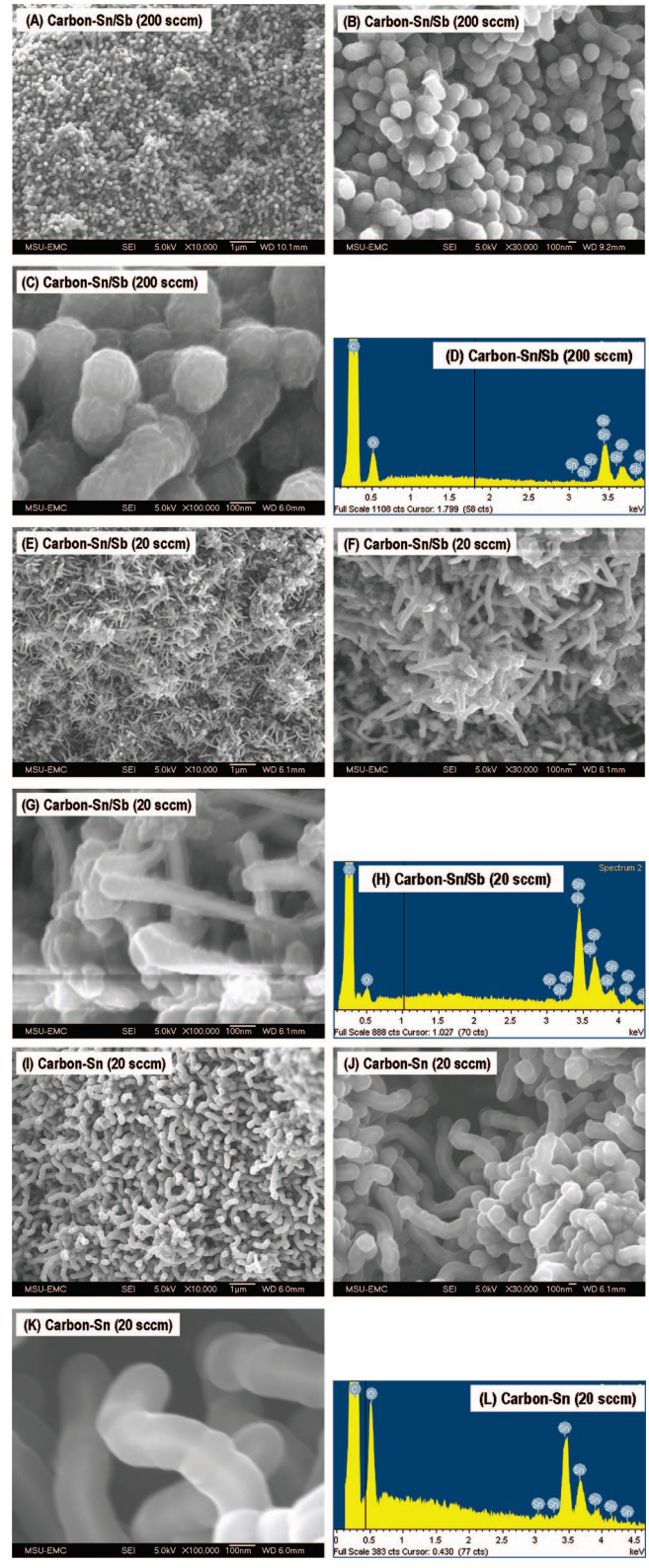

Figure 2. SEM images and X-EDS spectra of carbon-encapsulated metal nanorods; (A−D) carbon−Sn/Sb rods formed at 750 °C under C_2H_2 flowing at 200 sccm; (E−H) carbon−Sn/Sb rods formed at 750 °C under C_2H_2 flowing at 20 sccm; (I−L) carbon-encapsulated monometallic Sn nanorods formed at 750 °C in a 20 sccm C_2H_2 flow.

Table 1. X-EDS Elemental Analysis[a] and Thickness Ranges[b] of Carbon/Metal Nanorods Prepared at 750 °C for 4 h

	carbon−Sn/Sb	carbon−Sn/Sb	carbon−Sn
C_2H_2 flow rate (mL/min)	200	20	20
mole ratio of SnO_2:Sb_2O_5	0.9:0.1	0.9:0.1	
composition of feed	Sb_2O_5:7−11	Sb_2O_5:7−11	SnO_2:99.99
SnO_2 and Sb_2O_5 (wt %)	SnO_2:89−93	SnO_2:89−93	
C (wt %)[a]	77.10	51.89	82.50
O (wt %)[a]	4.43	2.13	4.82
Sn (wt %)[a]	17.71	41.63	12.68
Sb (wt %)[a]	0.77	4.35	0
total diameter range (nm)[b]	70−110	70−100	100−180
internal nanorod (Sn/Sb or Sb) diameter range (nm)[b]	20−40	50−80	80−140

[a] All elements analyzed by X-EDS. [b] All individual thickness observed by SEM and TEM.

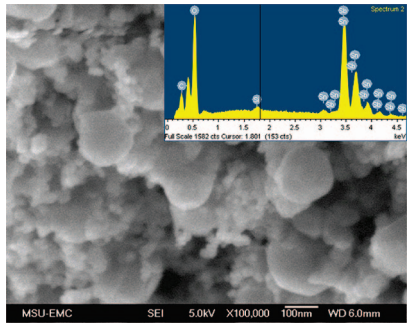

Figure 3. SEM image and X-EDS spectrum of the quasispherical nanoparticles of $Sb_2O_5 \cdot SnO_2$ formed on exposure to CH_4 (30 sccm) at 750 °C.

at 750 °C are shown in Figure 3. Tube-shaped products were not observed. Only spherical aggregated morphologies formed.

Transmission Electron Microscopy (TEM) Analyses. Rod morphologies were examined by TEM (Figure 4). These samples were produced at 750 °C. Many different views clearly revealed inner rodlike forms of Sn or Sn/Sb alloy encased in carbon. The mixed metal Sn/Sb rods will be discussed first. Figure 4A−C show the Sn/Sb nanorods formed under a 200 sccm, 10% C_2H_2/90% N_2 flow. The average overall diameter from examinations of many TEM images is about 105 nm. The thicknesses of the outer carbon layer is about 50−75 nm and the internal Sn/Sb alloy nanorods are 20−40 nm thick. In addition, the carbon surface is very rough. This is clearly seen in Figures 4A−C and less clearly in the SEM images (Figures 2A−C). Figures 4D−F display Sn/Sb nanorods formed at the lower, 20 sccm, acetylene flow rate after 4 h. The overall diameter of these tubes ranges from 70 to 100 nm, averaging ∼90 nm (versus ∼105 nm for tubes made at 200 sccm). The thickness of the outer carbon layer is about 20 nm and the Sn/Sb alloy nanorod diameters of 50−80 nm are about double those formed at the higher flow rate. Average thickness measurements are summarized in Table 1. These observations demonstrate that rod dimensions may be tailored by process variables.

Figures 4G−I show the core−shell structures of monometallic carbon-covered Sn nanorods formed at a 20 sccm flow rate. The inner Sn core and rough carbon surfaces are easily seen. The end tip regions of some rods exhibit carbon shells that are incompletely filled with Sn/Sb alloy or Sn. Others are completely filled with metal with no visible void space. An example of a hollow carbon tube with no metal core is shown in Figure 4(C). The monometallic (Sn) nanorods formed at 20 sccm flow rates exhibited greater overall diameters (100−180 nm) and thicker inner metallic Sn diameters (80−150 nm) than the Sn/Sb counterparts, especially those formed at higher flow rates (Figure 4, H versus B). A schematic illustration is shown in Figure 5 summarizing the variation of structure with acetylene flow rate at 750 °C. During Sn/Sb nanorod synthesis, a higher acetylene flow rate (200 sccm) increased the thickness of the outer carbon layer while the inner Sn/Sb nanorod is, on average, somewhat thinner than those formed at a lower (20 sccm) flow rate.

Effect of Raising the Reaction Temperature. Raising the reaction temperature to 810 °C in tin nanorod synthesis led to thicker overall total rod diameters (at a 30 sccm flow rate) due mainly to greater rates of outer layer carbon deposition (Table 2). After 4 h at 810 °C, the internal Sn rod diameters (70−100 nm) were somewhat smaller than those grown at 750 °C/20 sccm (80−140 nm). However, the overall diameters after 4 h at 810 °C were far larger (400−450 nm) than those grown at 750 °C (100−180 nm) due to a thicker outer carbon layer. The overall diameters at 810 °C grow from 110−120 nm after 1 h to 700−1000 nm after 8 h as the carbon layer thickened. These observations are reflected in the elemental compositions from X-EDS analysis. The Sn content dropped (62.8 to 9.8 wt %) and the carbon content increased (35.3 to 85.5 wt %) as the growth time increased from 1 to 8 h.

At 810 °C, the trends observed for bimetallic (Sn/Sb) nanorod growth were similar to those of the monometallic Sn rod, although the overall diameters were smaller, increasing from 50−130 nm at 1 h to 250−300 nm at 8 h (Table 3). The internal Sn/Sb rod diameters stay constant as the outer carbon layer grows thicker. This is also reflected in the metal content. The wt % Sn decreases (50 to 15) and carbon increases (42 to 82) between 1 and 8 h. After 8 h, Sb was not detected, but this is likely due to its low concentration and the sensitivity of X-EDS analysis.

At 810 °C, other morphologies besides the nanorods were also present in the carbon-encapsulated Sn material. Some spherical and hemispherical features and some lower-aspect-ratio, Christmas-tree-bulb-shaped budding rods were observed (Figure 6).

X-ray Diffraction (XRD) Analyses. Powder X-ray diffraction was performed to determine if the bi- and monometallic (Sn/Sb and Sn) nanorods within the carbon shells exhibited distinctive phases (Sn, Sn/Sb alloy, or SnO_2) (Figure 7). Diffraction patterns suggest the Sn/Sb rods formed at the 200 sccm flow rate contained both Sn and SnO_2. No peak for Sb or a Sn/Sb alloy was observed. The carbon−Sn/Sb rods prepared at a 20 sccm flow rate (thinner carbon layers, higher metal content) exhibited both Sn and Sn/Sb alloy phases and tin oxide. Finally, the carbon−Sn 20 sccm flow rate sample was found to contain Sn and SnO_2. The sharp peaks for Sn, Sn/Sb alloy, and SnO_2 shows that intermetallic nanorods contain well-crystallized structures. The SnO_2 may result from unreduced SnO_2 within the molten

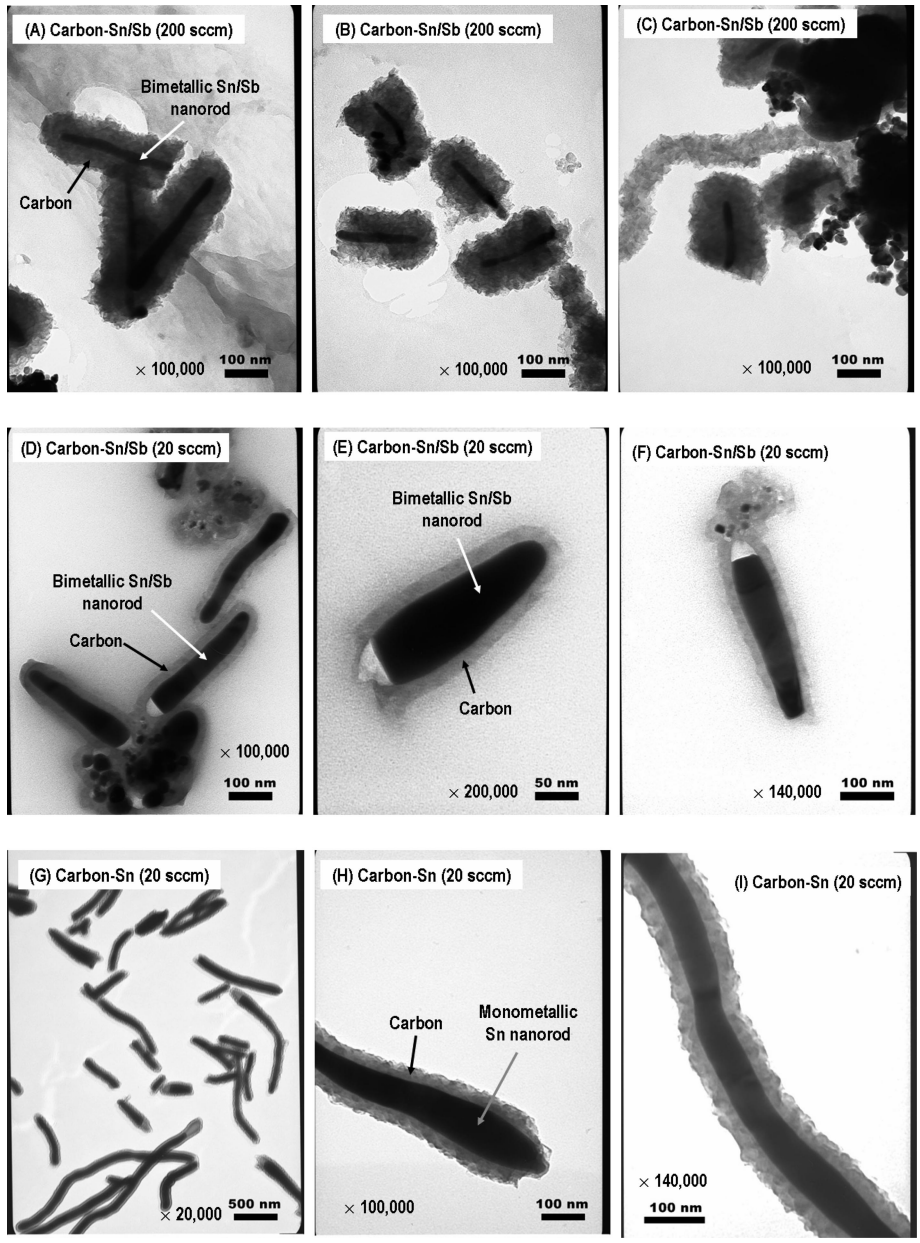

Figure 4. TEM images of carbon-encapsulated metal rods formed at 750 °C; (A−C) carbon−Sn/Sb rods formed under a 200 sccm C_2H_2 flow; (D−F) carbon−Sn/Sb rods formed under a 20 sccm C_2H_2 flow; (G−I) carbon monometallic Sn nanorods formed under a 20 sccm C_2H_2 flow.

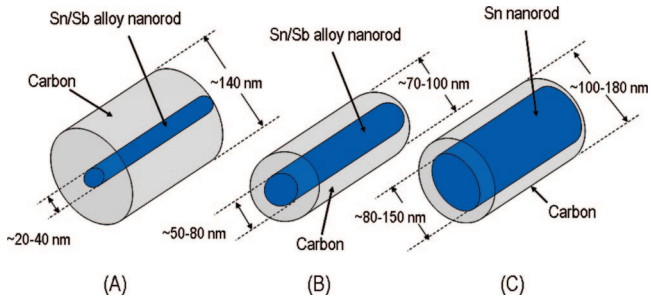

Figure 5. Illustration of the carbon-encapsulated Sn/Sb alloy or Sn nanorods formed at 750 °C under an acetylene flow rate of (A) 200 and (B) 20 sccm, respectively, and (C) 20 sccm.

Table 2. X-EDS Elemental Analysis and Thickness Ranges of Carbon/Tin Nanorods Prepared at 810 °C and a 30 sccm Flow Rate at Different Reaction Times

	growth period (h)		
	1	4	8
C (wt %)	35.34	56.06	85.51
Sn (wt %)	62.81	42.40	9.78
O (wt %)	0.66	2.24	4.70
diameter range of internal Sn rods (nm)	63−78	70−100	70−100
total rod diameter range (nm)	110−120	400−450	700−1000

Sn/Sb or Sn that is forced into growing carbon tubes or SnO_2 that lies in unreacted material contaminants at the base of the rods.

Sharp carbon XRD diffraction peaks from the outer shells were not found within the XRD patterns. However, a small broad diffraction peak with a low-intensity at $2\theta = 25°$ was observed that probably originates from the carbon shell (Figure 7). This is most easily observed in the Sn/Sb rods formed at an acetylene flow rate of 200 sccm. These had the thickest carbon shells. The lack of long-range order in the thin, short, and fractal carbon structures that make up the outer shells probably accounts for the lack of sharp

Table 3. X-EDS Elemental Analysis and Thickness Ranges of Sn/Sb Nanorod Samples Prepared at 810 °C and a Flow Rate of 30 sccm for Various Growth Times

	growth period for C/Sn/Sb system (h)		
	1	4	8
C (wt %)	42.11	70.11	82.22
Sn (wt %)	49.96	25.71	15.15
Sb (wt %)	5.73	2.56	1.40
O (wt %)	1.37	1.62	2.63
diameter range of internal metal rod (nm)	40−70	40−70	40−70
total diameter range of nanorods (nm)	50−130	100−145	250−300

Table 4. XRD Peak (2θ Scattering Angle) Assignments of Nanorod Samples Prepared at 750 °C

	carbon−Sn/Sb (200 sccm) (deg)	carbon−Sn/Sb (20 sccm) (deg)	carbon−Sn (20 sccm) (deg)
Sn	30.7	30.7	30.7
	32.1	32.1	32.1
	44.0	44.0	44.0
	45.0	45.0	45.0
Sn/Sb alloy		29.2	
		41.7	
SnO_2	38.3	38.3	38.3
possibly carbon	25.0 (broad)		

The XRD peak 2θ scattering angles were obtained from refs 24 and 26.

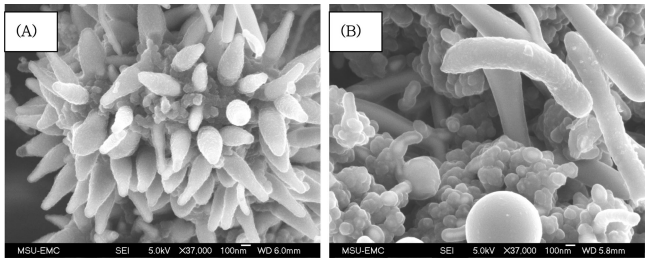

Figure 6. Additional morphologies observed in the Sn nanorod preparations at 810 °C at a 30 sccm flow rate. (A) Bulblike rods after 1 h. (B) Spherical and hemispherical buds with some rods after 4 h.

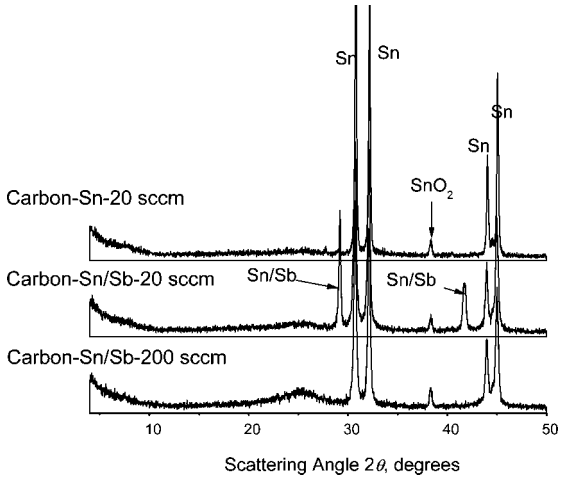

Figure 7. Powder X-ray diffraction (XRD) pattern of carbon-encapsulated Sn/Sb alloy nanorods formed under C_2H_2 flow rates of 200 and 20 sccm, respectively, and the carbon-encapsulated Sn nanorods formed at a 20 sccm flow rate. All samples were formed at 750 °C.

carbon peaks. The inability to observe Sn/Sb alloy diffraction peaks at $2\theta = \sim 29$ and $\sim 42°$ in the Sn/Sb structures formed at a 200 sccm flow rate is like due to the paucity of Sb

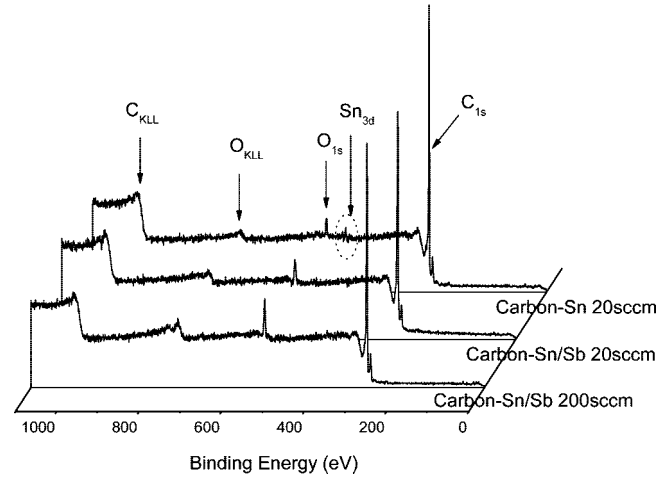

Figure 8. XPS wide-scan (low-resolution) spectra of carbon−Sn/Sb nanorods that formed at 750 °C under 200 and 20 sccm acetylene/nitrogen flows, respectively, and the carbon-encapsulated Sn nanorods formed at a 20 sccm flow rate.

present (0.77 wt %, Table 1). This peak was observed in the carbon−Sn/Sb (20 sccm) product where the sample contained over 4 wt % Sb. XRD peaks assignments are described and referenced in Table 2.[18,20]

X-ray Photoelectron Spectroscopy (XPS) Analyses. XPS analyses examined the C_{1s}, O_{1s}, and Sn_{3d} spectral regions to probe for these elements in the outer 50−100 Å (5−10 nm) surface region. Elements closer to the surface give greater responses. XPS experiments determined the presence and oxidation states of these elements in the nanorods. Figures 8 and 9 and Table 5 summarize the XPS results for the carbon−Sn/Sb-200 sccm, carbon−Sn/Sb-20 sccm, and carbon−Sn-20 sccm nanorod preparations at 750 °C.

Wide-scan (low-energy resolution) survey XPS spectra (Figure 8) were recorded from 0 to 1100 eV. Large C_{1s} and small O_{1s} and Sn_{3d} peaks were detected. The Sn_{3d} peak is very weak because Sn is encapsulated and few ejected electrons escape to the detector. The Sn_{3d} peak is seen where the outer carbon shells are thinnest, showing up in the Sn nanorods produced at 20 sccm acetylene flows. Sn or Sb peaks were not found in carbon−Sn/Sb nanorod products (produced at either 200 or 20 sccm). The carbon covering was thick enough that the Sn and Sb present inside did not appear.

XPS spectra measure the kinetic energy and number of electrons escaping from the top 1 to 10 nm of the material's surface. Metallic species (Sn/Sb alloy or Sn) only exist inside of the carbon tubes, so only a weak or no XPS spectral response is expected. The weak XPS response from Sn corresponds to a 0.3−0.6 wt % within the depth that is profiled for the Sn nanorods made at a 20 sccm flow rate.

(27) XPS database on Web: http://www.lasurface.com/database/elementxps.php (July 2007).
(28) XPS database on Web: http://srdata.nist.gov/xps/Elm_in_comp.htm (July 2007).
(29) Yue, Z. R.; Jiang, W.; Wang, L.; Gardner, S. D.; Pittman, C. U., Jr. *Carbon* **1999**, *37*, 1785.
(30) Lakshminarayanan, P. V.; Toghiani, H.; Pittman, C. U., Jr. *Carbon* **2004**, *42*, 2433.
(31) Gardner, S. D.; He, G.; Pittman, C. U., Jr. *Carbon* **1996**, *34*, 1221.

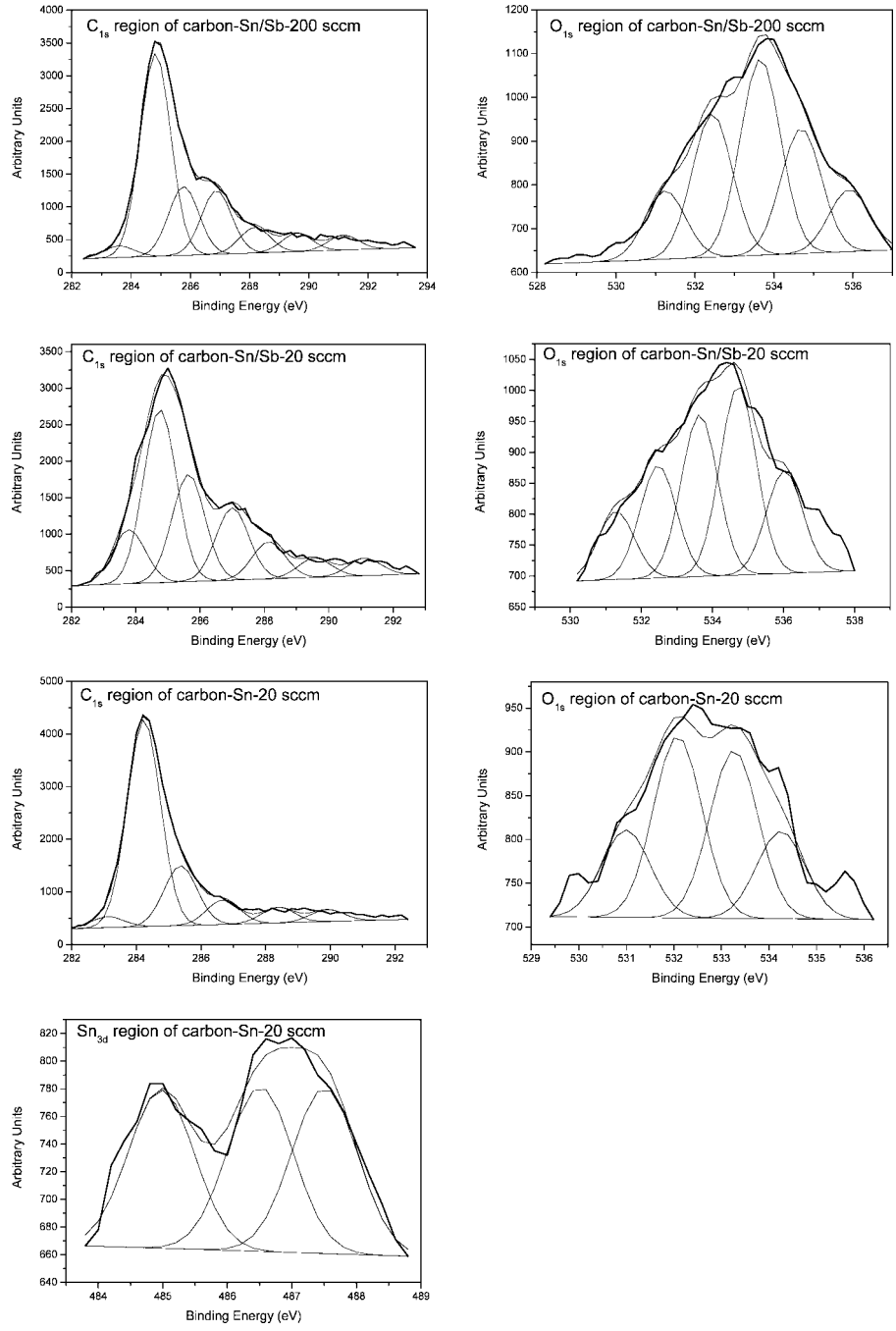

Figure 9. XPS high-resolution spectra of the C_{1s} and O_{1s} region of carbon−Sn/Sb nanorods that formed at 750 °C under 200 and 20 sccm C_2H_2 flow rates, respectively, and high-resolution spectra of the C_{1s}, O_{1s}, and Sn_{3d} regions of the carbon-encapsulated Sn nanorod formed at a 20 sccm flow rate. Real spectra (bold lines) and the curve-fitted spectra (nonbold lines) are overlaid.

The Sn_{3d} high-resolution spectrum is shown in Figure 9. The Sn_{3d} spectrum (Figure 8) was fitted to three 485.0, 486.5, and 487.5 eV peaks. These peaks are assigned to Sn metal and SnO_2, with the presence of SnO impossible to rule out.[27,28] XPS databases[27,28] summarize references to metallic Sn energies of 484.5, 484.7, and 484.9 eV. SnO_2 Sn_{3d} peaks have been reported[27] by various groups at 486.1, 486.4, 486.5, and 486.6 eV. Finally, peaks have been reported[27] for SnO at 486.3, 486.5, 486.7, and 486.8 eV in various studies. XRD (Figure 7) observed only SnO_2, but this does not rule out the presence of some SnO.

A pronounced O_{1s} response occurred from 530−538 eV. Where did this O_{1s} response originate from? A portion could come from unreduced SnO_2 or SnO_2/Sb_2O_5 remaining. However, this would lead to very small intensities. This suggests that oxidized carbon species are present in or on the nanorods, most likely concentrated at, or near, the outer surfaces. Thus, the XPS analysis of both O_{1s} and C_{1s} high-resolution spectra was conducted on the basis of our previous surface studies of oxidized carbon fibers and nanofibers[29−31] and those of others.[32,33] When carbon is formed at 700−800 °C from acetylene, the carbon surfaces must have unfilled

(32) Brisson, P.-Y.; Darmstadt, H.; Fafard, M.; Adnot, A.; Servant, G.; Soucy, G. *Carbon* **2006**, *44*, 1438.

(33) Wildgoose, G. G.; Lawrence, N. S.; Leventis, H. C.; Jiang, L.; Jones, T. G. J.; Compton, R. G. *J. Mater. Chem.* **2005**, *15*, 953.

Table 5. XPS Profile (C_{1s} and O_{1s} region) of Carbon−Sn/Sb Nanorods that Formed at 750 °C under C_2H_2 Flow Rates of 200 sccm (A) and 20 sccm (B), respectively, and C_{1s}, O_{1s}, and Sn_{3d} Regions of the Carbon-Encapsulated Sn Nanorod Formed at a C_2H_2 Flow Rate of 20 sccm (C)

peak	sample	binding energy (eV)	peak area percentage of the region (%)	peak area	chemical bonding[a]
C_{1s}-1	A[b]	283.59	2.9	303.1	diamond carbon
	B[b]	283.79	11.2	1259.3	
	C[b]	283.11	3.3	350.1	
C_{1s}-2	A	284.82	50	5268.6	graphite carbon
	B	284.75	36	4046.8	
	C	284.23	62.8	6703.7	
C_{1s}-3	A	285.77	17	1789.3	carbon present in phenolic, alcohol,
	B	285.64	22.3	2507	or ether groups
	C	285.36	18.1	1937	
C_{1s}-4	A	286.88	15.7	1654	carbonyl or quinone groups
	B	287	15.1	1690.8	
	C	286.69	7.5	796	
C_{1s}-5	A	288.18	6.4	669.9	carboxyl or ester groups
	B	288.14	7.7	868	
	C	288.39	4.7	505.3	
C_{1s}-6	A	289.6	4.5	476.6	carbon present in carbonate groups
	B	289.57	4	455	
	C	289.91	3.6	389.7	
C_{1s}-7	A	291.16	3.6	383.5	$\pi \rightarrow \pi^*$ (in C_6H_6)
	B	291.11	3.6	407	
	C				
O_{1s}-1	A	531.24	11.5	266.1	carbonyl oxygen of quinones
	B	531.29	10.7	187.3	
	C	530.99	16.7	170.3	
O_{1s}-2	A	532.44	24.1	557.4	carbonyl oxygen atoms in esters, anhydrides
	B	532.47	17.7	309.7	and oxygen atoms in hydroxyl groups
	C	532.08	34.6	353.9	
O_{1s}-3	A	533.66	33	764.6	noncarbonyl (ether type) oxygen atoms
	B	533.64	25.5	445.3	in esters and anhydrides
	C	533.26	32	327.1	
O_{1s}-4	A	534.69	21	487.1	oxygen atoms in carboxyl groups
	B	534.72	29.8	520.9	
	C	534.25	16.7	170.3	
O_{1s}-5	A	535.9	10.4	241.6	possibly some oxygen species in H_2O
	B	536.03	16.2	282.4	
	C				
Sn_{3d}-1	C	484.98	32.4	195.2	Sn metal
Sn_{3d}-2	C	486.51	33.7	202.6	SnO_2
Sn_{3d}-3	C	487.51	33.9	204.1	SnO

[a] The XPS profile of the chemical and oxidation state was investigated by XPS database on Web[27,28] and other literature.[29−33] [b] A, B, and C stand for the samples shown at the flow rates with the corresponding letter designations in the title.

valences and radical sites. Upon admitting air to the reactor, oxygen will react at these sites. The high-resolution spectrum of the O_{1s} region of carbon−Sn nanorods is illustrated in Figure 9. This was fitted to five peaks, all of which correspond to oxygens in oxidized carbon functional groups (carboxyl, ester, anhydride, keto, ether and hydroxyl). Positions are described and referenced in Table 5.

Figure 9 also displays the high resolution spectrum of the C_{1s} region of carbon-Sn/Sb nanorods that formed under 200 and 20 sccm acetylene flow rates, respectively. Each spectrum was fitted to seven peaks including unoxidized diamond (sp^3) and graphitic (sp^2) carbon. The typical peak positions correspond to different carbon oxidation states (Table 5). A large peak (at 284.82 and 284.75 eV in both spectra) is attributed to the graphitic carbon containing a polyaromatic layered structure. In addition, two $\pi \rightarrow \pi^*$ aromatic graphitic peaks (at 291.16 and 291.11 eV), and two small peaks (283.59 and 283.79 eV with areas of 2.9 and 11.2%, respectively) are assigned to diamond-like (extended sp^3) carbon. Thus, a small amount of a tetrahedral carbon is present. Various oxidized carbon functions were found (C_{1s} peaks 3−7 in Table 5). These were assigned to oxidized carbon present in phenolic, alcohol, or ether groups (peak 3), carbonyl or quinone groups (peak 4), carboxyl anhydride or ester groups (peak 5), and carbonate groups (peak 6), which formed on exposure of the newly formed nanorods to air. Overall, XPS measurements confirm that the outer carbon regions of carbon−Sn/Sb and carbon−Sn nanorods are composed mostly of unoxidized graphite-like carbon, with a small fraction of tetrahedral carbon present together with an oxidized carbon surface region.

Elemental Analysis. Carbon, tin, and antimony elemental analysis of the core−shell nanorods were performed at Galbraith Laboratory, Knoxville, TN (Table 6). The carbon−Sn/Sb nanorod sample prepared at an acetylene flow rate of 20 sccm exhibited C, 63.35%, Sn, 11.80%, Sb, 1.22% (the Sn:Sb atomic ratio of 9.7:1 agrees well with the 8.7−14.3 ratio in the commercial antimony tin oxide nanopowder). This suggests that no selective incorporation of either Sn or Sb into the carbon interior had occurred. The carbon−Sn (20 sccm) nanorod sample exhibited 19.6% Sn, in crude agreement with X-EDS measurements (Sn, 12.68%) (Table 1). However, the carbon−Sn/Sb nanorod sample prepared at a 200 sccm flow rate exhibited much smaller amounts of the metals (Sn 5.99% and Sb 0.283%; Sn/Sb = 21.7) than X-EDS measurements (Sn 17.71% and Sb 0.77%, Sn/Sb = 23.6). The Sn:Sb atomic ratios from both Galbraith and X-EDS (21.7 and 23.6, respectively) were in poor

Table 6. Elemental (Carbon, Tin, and Antimony) Analysis of the Nanorods

samples	analysis	commercial results[a] (%)	X-EDS results[b]
carbon−Sn/Sb (200 sccm)	C	79.46	77.10
	Sn	5.99	17.71
	Sb	0.28	0.77
carbon−Sn/Sb (20 sccm)	C	63.35	51.89
	Sn	11.80	41.63
	Sb	1.22	4.35
carbon−Sn (20 sccm)	C	54.48	82.50
	Sn	19.6	12.68

[a] Carbon, tin, and antimony elemental analysis of the core−shell nanorods were performed at Galbraith Laboratory on representative weight fractions of the entire reaction products. [b] Elemental analysis were performed by X-EDS (see Table 1). These depend on the spot location and the sample penetration depth.

agreement with the 9.7:1 Sn:Sb ratio in the precursor oxides. Commercial analyses required complete carbon oxidation and metal dissolution.

Conclusions

Two types of carbon-encapsulated mono- and bimetallic (Sn and Sn/Sb alloy) nanorods were successfully synthesized by a thermochemical vapor deposition of carbon and reduction of commercial Sb_2O_5/SnO_2 or SnO_2 nanoparticles in an acetylene/nitrogen flow at temperatures from 750 to 810 °C. Bimetallic Sn/Sb alloy and monometallic Sn nanorods formed inside hollow carbon tubular outer layers through capillary uptake of the molten metals formed by metal oxide reduction. The nanorods morphologies and structures were observed in SEM and TEM images. The overall nanorod thicknesses and the internal metal diameter were varied by changing the acetylene flow rates. Higher flow rate (200 sccm) increases the thickness of outer carbon layers, whereas the inner Sn/Sb nanorod is, on average, somewhat thinner than nanorods formed at a lower (20 sccm) flow rate. Attempts to synthesize bimetallic carbon-encased nanorods using a methane flow (10% CH_4 and 90% N_2) at 750 °C were unsuccessful.

Powder X-ray diffraction proved that the Sn and Sn/Sb alloys formed inside the hollow carbon shells and detected some unreduced SnO and SnO_2. The sharp XRD peaks showed that nanorods had well-crystallized metal structures. XPS showed that the carbon was mostly graphitic but some tetrahedral (sp^3) carbon was also present. XRD Peaks for various carbon oxidation states were found, indicating the presence of oxygen-containing carbon functional groups (carboxyl, ester, anhydride, ketone, alcohol, ether, and carbonate) on the carbon surfaces. Phenolic alcohol and/or ether groups were indicated at binding energies of ∼285.7 eV, carbonyl or quinone groups at ∼286.9 eV, carboxyl and/or ester and anhydride groups at 288.1 eV, and carbonate groups at ∼289.5 eV.

The surface conductivity of the carbon coatings, the very high surface areas, and ability of Sn or Sb to alloy with Li and the ability of Li to intercalate into graphitic carbon to give $Li^+C_x^-$ ($x \geq 6$) suggest these nanorods could be used as anode materials in rechargeable lithium-ion batteries.

Acknowledgment. The U.S.Army, CERDEC, Army Power Division, provided financial support through Contract W15P7T-06−C-P408. Supplemental funding was provided by the Office of Research, Mississippi State University.

CM900640U